Direct numerical simulation of self-similar turbulent boundary layers in adverse pressure gradients

By Martin Skote[*], Dan S. Henningson[*†] and Ruud A. W. M. Henkes[‡]

Direct numerical simulations of the Navier-Stokes equations have been carried out with the objective of studying turbulent boundary layers in adverse pressure gradients. The boundary layer flows concerned are of the equilibrium type which makes the analysis simpler and the results can be compared with earlier experiments and simulations. This type of turbulent boundary layers also permits an analysis of the equation of motion to predict separation. The linear analysis based on the assumption of asymptotically high Reynolds number gives results that are not applicable to finite Reynolds number flows. A different non-linear approach is presented to obtain a useful relation between the freestream variation and other mean flow parameters. Comparison of turbulent statistics from the zero pressure gradient case and two adverse pressure gradient cases shows the development of an outer peak in the turbulent energy in agreement with experiment. The turbulent flows have also been investigated using a differential Reynolds stress model. Profiles for velocity and turbulence quantities obtained from the direct numerical simulations were used as initial data. The initial transients in the model predictions vanished rapidly. The model predictions are compared with the direct simulations and low Reynolds number effects are investigated.

1. Introduction

The analysis of adverse pressure gradient (APG) turbulent boundary layers has been going on for a long time. Disagreement in the approach of analysis as well as contradiction in results from experiments are found in the literature. Only in recent years have direct numerical simulations (DNS) of these flows become possible, albeit for low Reynolds numbers.

The conditions needed for self-similarity as well as for the onset of separation have been the subject of several investigations. Clauser (1954) performed

[*]Department of Mechanics, Royal Institute of Technology (KTH), SE-100 44 Stockholm, Sweden
[†]Aeronautical Research Institute of Sweden (FFA), Box 11021, SE-161 11 Bromma, Sweden
[‡]Shell Research and Technology Centre Amsterdam, P.O. Box 3003, 1003 AA Amsterdam, The Netherlands

experiments where he adjusted the pressure gradient such that a self-similar turbulent boundary layer was obtained. A constant non-dimensional pressure gradient,

$$\beta = \frac{\delta^*}{\tau_w}\frac{dP}{dx},$$

was shown to be a condition for self-similarity. Here δ^* is the displacement thickness, τ_w is the wall shear stress and dP/dx is the pressure gradient. Townsend (1976) and Mellor & Gibson (1966) showed that self-similarity is obtained if the freestream variation has the form of a power law in the downstream direction, $U \sim x^m$, where U is the freestream velocity and x is the streamwise coordinate. Townsend used non-specified length and velocity scales and analyzed the equation describing the outer part of the turbulent boundary layer. His analysis showed that in addition to the condition $U \sim x^m$ the length scale must vary linearly with the downstream coordinate. Mellor & Gibson analyzed the integrated momentum equation with the length and velocity scales $\Delta = (U/u_\tau)\delta^*$ and u_τ, where u_τ is the friction velocity. Under certain approximations they obtain that for flows with $\beta =$ const. the freestream variation is $U \sim x^m$ and $\Delta \sim x$. Tennekes & Lumley (1972) analyzed the integrated momentum equation with an assumption of sufficiently high Reynolds number, so that the velocity defect law could be linearized, and they obtained a relation between the exponent and Clauser's non-dimensional pressure gradient β which reads

$$m = -\frac{\beta}{1+3\beta}.$$

Following Clauser, a number of measurements have been carried out in self-similar adverse pressure gradient turbulent boundary layers near separation. Bradshaw (1967) measured three self-similar turbulent boundary layers with $m = 0, -0.15, -0.255$. In the last case the turbulence intensities showed peak values in the outer part of the layer and the boundary layer was near separation. Skåre & Krogstad (1994) experiments near separation showed that the shape factor approaches 2 and $m = -0.22$. In their experiments $\beta = 20$ and the shape factor as well as the ratio u_τ/U was found to be constant. They also obtained self-similar velocity profiles. Stratford (1959*a*) performed measurements on a turbulent boundary layer near separation as well as an analysis of the inner and outer equations (Stratford 1959*b*). He concluded that the asymptotic form of the separation profile near the wall is proportional to $y^{1/2}$, which was also theoretically verified by Durbin & Belcher (1992).

The value of m near separation has also been investigated theoretically. Head (1976) used an integral method to calculate the turbulent boundary layer for $m = -0.15, -0.255, -0.35$ and concluded that the solution is unique in the first case whereas multiple solutions exist in the second. No solution was obtained in the third case. Schofield (1981) analyzed the self-similar boundary layers based on the Schofield-Perry law. He concluded that there is no solution for $m < -0.3$ and only one solution exists for $m > -0.23$.

In recent years direct numerical simulations of turbulent boundary layers have become an important complement to experiments. Spalart (1988) carried out DNS of a zero pressure gradient turbulent boundary layer. Spalart & Leonard (1987) performed DNS of self-similar APG turbulent boundary layer using a similarity coordinate system. In these simulations the shape factor approaches 2.3 and $m = -0.22$ near separation. Spalart & Watmuff (1993) compared experiments and DNS of an APG turbulent boundary layer in a varying pressure gradient and they found good agreement. Recent simulations have also been made past the point of separation. Coleman & Spalart (1993) and Spalart & Coleman (1997) performed DNS of a separation bubble with heat transfer. Na & Moin (1996) have performed DNS of a separation bubble and they presented the Reynolds stresses and turbulent energy budgets.

Regarding self-similar adverse pressure gradient turbulent boundary layer, both theoretical work and experiments support the idea that a power law freestream velocity is a requirement for self-similarity. The assumption of infinite Reynolds number and the use of specific velocity and length scales have given a relation between m and β. The consensus from the experiments and DNS performed for turbulent boundary layers near separations seems to be that separation occurs for about $-0.25 < m < -0.20$ with a shape factor of about 2.

The work presented here starts in section 2 with an introduction to the concept of self-similarity of turbulent boundary layers subjected to adverse pressure gradients. A relation between the non-dimensional pressure gradient and m is also derived. The numerical code for the turbulence model prediction and the code for the DNS is described in section 3. Section 4 is devoted to results from the DNS as well as comparison with turbulence model predictions. In section 5 we sum up and draw conclusions.

2. Analysis of the turbulent boundary layer equations

The first part of this section consists of a review of the asymptotic behavior of adverse pressure gradient boundary layer flows. In the second part the analysis is extended and the restriction to asymptotically high Reynolds number is relaxed, and in the last part the relation to earlier work is discussed.

2.1. *Linearized analysis*

The equations for an incompressible two-dimensional turbulent boundary layer are

$$\frac{\partial u}{\partial x} + \frac{\partial v}{\partial y} = 0 \tag{1}$$

$$u\frac{\partial u}{\partial x} + v\frac{\partial u}{\partial y} = -\frac{1}{\rho}\frac{dP}{dx} + \nu\frac{\partial^2 u}{\partial y^2} - \frac{\partial}{\partial y}\langle u'v'\rangle \tag{2}$$

where u is the mean streamwise velocity, v the mean wall normal velocity, dP/dx the pressure gradient, $\langle u'v'\rangle$ the Reynolds stress, ρ the density and ν

the kinematic viscosity. If the pressure gradient is not too large, the scalings in the inner part of the boundary layer remain the same as in the zero pressure gradient case. For the outer part however, the analysis must take into account even a weak pressure gradient. The equation describing the outer part of an incompressible turbulent boundary layer is given by

$$u\frac{\partial u}{\partial x} + v\frac{\partial u}{\partial y} = -\frac{1}{\rho}\frac{dP}{dx} - \frac{\partial}{\partial y}\langle u'v'\rangle. \tag{3}$$

A self-similar solution has no explicit dependence on x. Thus we seek solutions of the form

$$(u-U)/u_\tau = F(\eta), \qquad -\langle u'v'\rangle/{u_\tau}^2 = R(\eta), \tag{4}$$

where

$$\eta = y/\Delta(x), \qquad \Delta = U\delta^*/u_\tau. \tag{5}$$

Substituting these expressions into equation (3) we obtain

$$-2\beta F - (1+2\beta)\eta\frac{dF}{d\eta} = \frac{dR}{d\eta}, \tag{6}$$

when $u_\tau/U \to 0$. The classical treatment of the equations which involves outer and inner equations and a matching of the solutions, leads to the logarithmic friction law,

$$\frac{u_\tau}{U} = \frac{1}{C + \frac{1}{\kappa} ln Re_{\delta^*}}, \tag{7}$$

where κ is the Kármán constant and $Re_{\delta^*} = U\delta^*/\nu$. Equation (7) shows that $u_\tau/U \to 0$ in the limit of very high Reynolds number, which is utilized in the derivation of equation (6). This derivation is given in different ways by Tennekes & Lumley (1972), Mellor & Gibson (1966) and Henkes (1998).

From equation (6) one obtains a condition for self-similarity as a parameter β that should be constant

$$\beta = \frac{\delta^*}{\tau_w}\frac{dP}{dx}. \tag{8}$$

That β should be constant follows from a balance of the skin friction force and the pressure gradient force, as argued by Clauser (1954).

Assuming a self-similar boundary layer, we proceed to give the Tennekes & Lumley (1972) analysis resulting in a relationship between β and m. We start with the integrated momentum equation,

$$\left(\frac{U}{u_\tau}\right)^2 \frac{d}{dx}\Theta - \frac{2\beta}{H} = 1 + \beta, \tag{9}$$

which is equation (2) integrated from the wall to the freestream. We rewrite the velocity defect term as

$$u(U-u) = U(U-u) - (U-u)^2. \tag{10}$$

If the velocity defect is assumed to be of order u_τ, the last term is an order u_τ/U smaller than the others and can be neglected, giving

$$\frac{u}{U}\left(1-\frac{u}{U}\right) \rightarrow \left(1-\frac{u}{U}\right) \tag{11}$$

if $u_\tau/U \rightarrow 0$. From this equation it is clear that the linearization is equivalent to the assumption of a shape factor equal to unity since $\Theta = \delta^*$. The linearized version of equation (9) thus becomes

$$\frac{U}{{u_\tau}^2}\frac{d}{dx}(\Delta u_\tau) = 1 + 2\beta. \tag{12}$$

By keeping the ratio u_τ/U approximately constant in equation (12) Tennekes & Lumley obtain a relation between m and β which reads

$$m = -\frac{\beta}{1+3\beta} \tag{13}$$

with

$$U \sim x^m. \tag{14}$$

2.2. *Non-linear analysis*

A shape factor equal to unity is an unrealistic approximation in most practical cases, see Fernholz & Finley (1996) for an assessment of data from experiments on zero pressure gradient turbulent boundary layers. Since we are interested in using a relation such as (13) for separation prediction it would be useful to obtain results that are not restricted to asymptotically high Reynolds numbers. We will now derive a relation between β and m without this restriction.

The full integrated momentum equation (9) can be written as

$$\frac{U'\delta^*}{U{\delta^*}'} = -\frac{\beta}{H(1+\beta)+2\beta+(H-1)\beta(1-\frac{{u_\tau}'U}{u_\tau U'})}, \tag{15}$$

where the $'$ denotes x-derivative. We have used the relation

$$H = \frac{1}{1-\frac{u_\tau}{U}G} \tag{16}$$

with

$$G = \int_0^\infty F^2 d\eta. \tag{17}$$

G must be constant if the boundary layer is to be self-similar, i.e. F does not change its shape. From equation (16) the limit $H \rightarrow 1$ as $u_\tau/U \rightarrow 0$ is consistent with the linearization (11) described above. The use of the limit value $u_\tau/U \rightarrow 0$ as $Re \rightarrow \infty$ is motivated by equation (7). Since the logarithmic function grows very slowly when the argument is large, a better assumption than $u_\tau/U \rightarrow 0$ for moderately high Reynolds numbers is that $u_\tau/U \approx$ constant, which is consistent with many of the numerical investigations and experiments described in the introduction. If u_τ/U is kept constant, which implies that

$$\frac{u_\tau' U}{u_\tau U'} = 1, \tag{18}$$

equation (15) can be written as

$$\frac{U'\delta^*}{U\delta^{*\prime}} = -\frac{\beta}{H(1+\beta)+2\beta} = m. \tag{19}$$

Equation (19) can be integrated to give

$$\frac{U}{U_0} = \left(\frac{\delta^*}{\delta_0^*}\right)^m, \tag{20}$$

where the subscript 0 refers to the initial values at $x = 0$ The definition of β, equation (8), can be written as

$$\beta = -\frac{\delta^*}{u_\tau^2} U \frac{dU}{dx}. \tag{21}$$

Combining equations (20) and (21) and integrating gives

$$\frac{U}{U_0} = \left[1 - \frac{\beta}{m\delta_0^*}\left(\frac{u_\tau}{U}\right)^2 x\right]^m \tag{22}$$

and

$$\frac{\delta^*}{\delta_0^*} = 1 - \frac{\beta}{m\delta_0^*}\left(\frac{u_\tau}{U}\right)^2 x. \tag{23}$$

Introducing x_0 as a virtual leading edge where $\delta^* = 0$ we derive from equation (23) that

$$\delta_0^* = \frac{\beta}{m}\left(\frac{u_\tau}{U}\right)^2 x_0. \tag{24}$$

Using equation (24), the equations (22) and (23) can be written as

$$\frac{U}{U_0} = \left(1 - \frac{x}{x_0}\right)^m, \qquad \frac{\delta^*}{\delta_0^*} = 1 - \frac{x}{x_0}. \tag{25}$$

The result is that

$$U \sim x^m, \qquad \delta^* \sim x, \tag{26}$$

with

$$m = -\frac{\beta}{H(1+\beta)+2\beta}. \tag{27}$$

Equation (13) is recovered from equation (27) by setting $H = 1$.

In section 4.2.2 a comparison between the relations (13) and (27) will show that the linearization, which might be correct for asymptotically high Reynolds number, is insufficient for low and moderate Reynolds number flows.

2.3. *Relation to previous work*

Equation (15) can be integrated if the right hand side is assumed to be constant. This was done by Mellor & Gibson (1966) who found that

$$U \sim \tilde{x}^m \tag{28}$$

with

$$\tilde{x} = \int_0^x \frac{u_\tau U_0}{u_{\tau 0} U} dx, \tag{29}$$

where m in their case is equal to the right hand side of equation (15). With $u_\tau/U = \text{const.}$ the variable $\tilde{x}$ in equation (28) becomes x and the results in equations (26) and (27) are recovered. Due to the slow increase of $\ln(Re)$ with Re, H and u_τ/U are far from their asymptotic values of 1 and 0 respectively in many experiments and DNS. They are on the other hand fairly constant in a large range of Reynolds numbers for the same reason. Thus it seems as equations (28) and (29) do not add substantially new information to the non-linear theory with a constant u_τ/U as an approximation.

The relation (27) was obtained by Rotta (1962), although expressed in G and u_τ/U. This work was apparently unnoticed by Townsend (1976) and Mellor & Gibson (1966), whose work is closely related to Rotta's.

An alternative to the procedure of letting $u_\tau/U \to 0$ for high Reynolds numbers to obtain self-similar equations, is to scale the velocity defect with U instead of u_τ to obtain full similarity of equation (3). This is done by George & Castillo (1993). One of the consequences is that the logarithmic region in the velocity profile is substituted by a power law region. The same scaling was used by Townsend (1960) for the near separation case, where he also used the half-power law, $u \sim y^{1/2}$, of Stratford (1959*b*). He develops a theory to predict the experiment by Stratford (1959*a*) with the assumption of constant eddy viscosity. To predict the velocity profile Townsend had to change the values of measured constants in his calculations, e.g. the exponent m is 0.234 instead of the measured 0.25.

Using the constraint $u_\tau/U = \text{const.}$ together with $U \sim x^m$ in equation (3) gives instead of equation (6) the following equation

$$2mF - (1+m)\eta\frac{dF}{d\eta} - \frac{u_\tau}{U}(1+m)\frac{dF}{d\eta}\int_0^\eta F d\eta + \frac{u_\tau}{U}mF^2 = -\frac{dR}{d\eta}\frac{m}{\beta}. \quad (30)$$

Integrating this equation gives $m = -1/(H+2)$ which is the same as relation (27) for $\beta \to \infty$. In equation (30) the viscous term is neglected, which means that $\nu(\partial u/\partial y)(y=0) = 0$, i.e. we implicitly obtain the case at separation. Adding the viscous term, which reads

$$\nu\frac{d^2F}{d\eta^2}\frac{1}{\Delta u_\tau}\frac{m}{\beta}, \quad (31)$$

to the right hand side of equation (30) and integrating gives the relation

$$m = -\frac{\beta}{H(1+\beta)+2\beta},$$

which is the same as (27). In the integrations above the following relations have been used,

$$-\int_0^\infty F d\eta = \int_0^\infty \eta\frac{dF}{d\eta}d\eta = 1, \quad (32)$$

$$\int_0^\infty F^2 d\eta = -\int_0^\infty \left(\frac{dF}{d\eta}\int_0^\eta F d\eta\right)d\eta = \frac{H-1}{H\frac{u_\tau}{U}}. \quad (33)$$

3. Computational tools and parameters

3.1. *The DNS Code*

The code used for the direct numerical simulations (DNS) is developed at KTH and FFA (Lundbladh *et al.* 1992, 1994). The numerical approximation consists of spectral methods with Fourier discretization in the horizontal directions and Chebyshev discretization in the normal direction. Since the boundary layer is developing in the downstream direction, it is necessary to use non-periodic boundary conditions in the streamwise direction. This is possible while retaining the Fourier discretization if a fringe region is added downstream of the physical domain. In the fringe region the flow is forced from the outflow of the physical domain to the inflow. In this way the physical domain and the fringe region together satisfy periodic boundary conditions. The fringe region is implemented by the addition of a volume force F, to the Navier-Stokes equations:

$$\frac{\partial u_i}{\partial t} + u_j \frac{\partial u_i}{\partial x_j} = -\frac{1}{\rho}\frac{\partial p}{\partial x_i} + \nu \frac{\partial^2 u_i}{\partial {x_j}^2} + F_i. \tag{34}$$

The force

$$F_i = \lambda(x)(\tilde{u}_i - u_i) \tag{35}$$

is non-zero only in the fringe region; $\tilde{u}_i$ is the laminar inflow velocity profile the solution u_i is forced to and $\lambda(x)$ is the strength of the forcing with a maximum of about 1. The form of $\lambda(x)$ is designed to minimize the upstream influence and is sketched in Figure 1. The figure shows the whole computational box with the fringe region at the end. The dotted line shows how the boundary layer grows downstream and is forced back to its inflow value in the fringe region. The forcing at the beginning of the fringe region is towards the boundary layer as it would continue downstream. This is done to damp the disturbances before the actual forcing towards the inflow profile starts. See Nordström *et al.* (1999) for an investigation of the fringe region technique.

Time integration is performed using a third order Runge-Kutta method for the advective and forcing terms and Crank-Nicolson for the viscous terms. A 2/3-dealizing rule is used in the streamwise and spanwise direction.

3.2. *Numerical parameters*

Results from two direct numerical simulations of APG turbulent boundary layers as well as one zero pressure gradient case (ZPG) are presented. In the first APG case (APG1) the pressure gradient is close to that for which the corresponding laminar boundary layer would separate and in the second case (APG2) the pressure gradient is the same as in Bradshaw's first experimental APG case (Bradshaw 1967). The pressure gradient is applied through the variation of the freestream velocity, which is described by a power law, $U \sim x^m$. For APG1 $m = -0.077$ and for APG2 $m = -0.15$, which corresponds to $\beta \approx 0.24$ and $\beta \approx 0.65$ respectively. The results from the ZPG are taken from a simulation by Henningson & Lundbladh (1995). This simulation was done

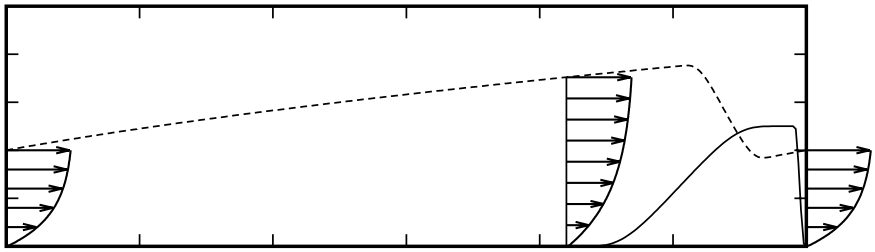

FIGURE 1. Computational box with the fringe region — $\lambda(x)$, the fringe function. - - the boundary layer thickness.

with a different set of parameters, see Table 1, and is not as highly resolved as the other two. The results are included only as a comparison to the two APG simulations. The simulations start with a laminar boundary layer at the inflow which is triggered to transition by a random volume force near the wall. All the quantities are non-dimensionalized by the freestream velocity (U) and the displacement thickness (δ^*) at the starting position of the simulation ($x = 0$) where the flow is laminar. At that position $Re_{\delta^*} = 400$. The length (including the fringe), height and width of the computation box were $450 \times 24 \times 24$ in these units for the largest case, APG2. The number of modes in this simulation was $480 \times 161 \times 96$, which gives a total of 7.5 million modes or 17 million collocation points. For comparison with the other cases, see Table 1. In all simulations the fringe region has a length of 50 and the trip is located at $x = 10$. The useful region starts at $x = 150$, which corresponds to different values of Re_Θ as also found in Table 1.

The simulations were run for a total of 4500 time units (δ^*/U), and the sampling for the turbulent statistics was performed during the 2000 last time units. It was verified that the accuracy of the DNS and its statistics was sufficient by repeating the computation of the APG1 case on a coarser resolution ($320 \times 101 \times 64$ modes) and with a shorter averaging time (1000 time units), see Henkes *et al.* (1997). The differences between the two resolutions are shown in Figures 2a and 2b, where the mean velocity and Reynolds stresses are shown. The difference between the coarser grid case (APG1a) and the full resolution case (APG1) is small even though the number of points is reduced by a factor of almost 2/3 in all directions. The resolutions of the cases APG1 and APG2 were thus considered to be sufficient.

Case	L_x	L_y	L_z	NX	NY	NZ	ΔX^+	ΔZ^+	Useful region, Re_Θ
ZPG	500	12	25	320	81	64	31	7.8	$350 - 525$
APG1a	450	18	24	320	101	64	24	6.5	$390 - 620$
APG1	450	18	24	480	121	96	16	4.3	$390 - 620$
APG2	450	24	24	480	161	96	13	3.6	$430 - 690$

TABLE 1. Numerical parameters.

3.3. *The turbulent boundary layer code*

To be able to investigate the relevance of the asymptotic analysis described above the use of turbulence models is the only option. Direct numerical simulation is possible only for low Reynolds number flows and experiments are performed at higher, but not high enough Reynolds number for the full asymptotic behavior to appear. We will also use model predictions at low Reynolds number for comparison with DNS. It is possible to draw conclusions about the low Reynolds number effects in the DNS data by comparing model predictions at low and high Reynolds numbers.

The equations solved are (1) and (2) together with a closure for the Reynolds shear tress $\langle u'v' \rangle$. In the calculations described here the Differential Reynolds Stress Model of Hanjalić *et al.* (1995) is used. The model contains transport equations for the Reynolds stresses, the turbulent kinetic energy and the dissipation rate, see Appendix A. The ϵ equation contains a source term

$$S_{\epsilon 4} = C_{\epsilon 4} \frac{\epsilon}{k} \left(\langle v'^2 \rangle - \langle u'^2 \rangle \right) \frac{\partial u}{\partial x}, \tag{36}$$

where ϵ is the dissipation rate, k the turbulent kinetic energy, $\langle u'^2 \rangle$ and $\langle v'^2 \rangle$ the streamwise and normal Reynolds stresses and $C_{\epsilon 4}$ a constant. The term (36) is a simplified version of the original term and introduced by Hanjalić & Launder (1980). They also showed that (36) gives a significant contribution to the ϵ equation in boundary layer flows with streamwise pressure gradient. For a complete description of the model, see Henkes (1997). The calculations were made with a parabolic boundary layer code. The discretization is based on the finite volume method with a second-order upwind scheme in the downstream direction. In the normal direction is either a central scheme or a first-order upwind scheme used, depending on the ratio between the convection and diffusion term. The grid is uniform in the downstream direction but stretched in the normal direction. To account for the growth of the boundary layer in the downstream direction, at several x positions the outer edge was increased and the y grid points were redistributed. All the calculations presented in this paper have been checked to be grid independent. This was done by doubling the number of points in the x and y directions.

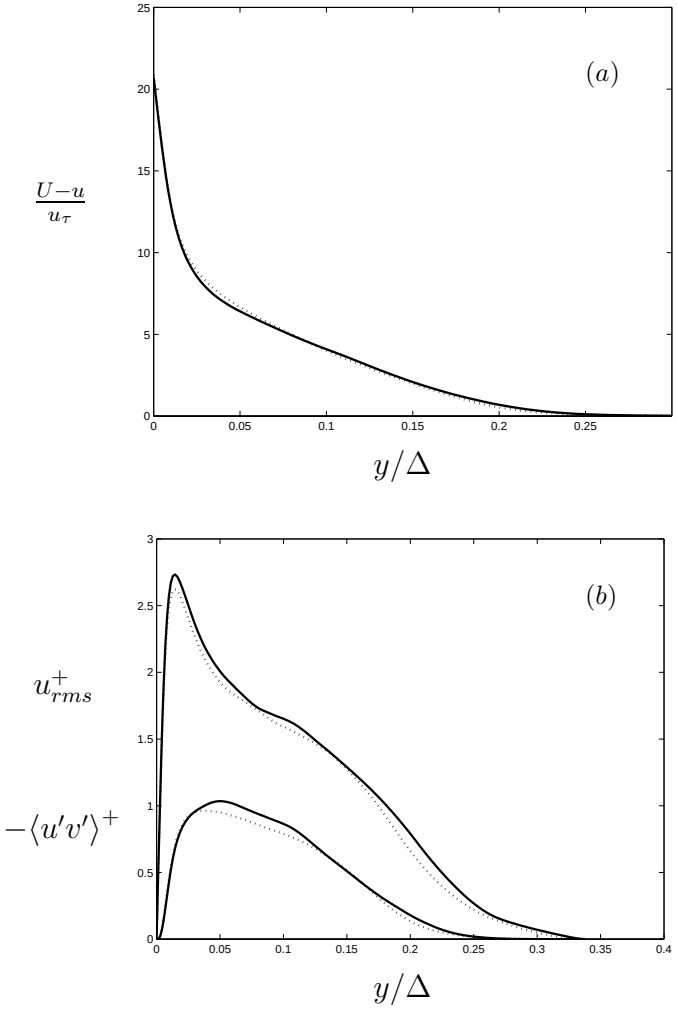

FIGURE 2. (a) Velocity defect. (b) u^+_{rms} and Reynolds stress for — $480 \times 121 \times 96$; $\cdots$ $320 \times 101 \times 64$.

4. DNS Results

In this section the results from the direct numerical simulations are presented. Section 4.1 deals with the flow structures. The downstream behavior of the mean flow quantities is described in section 4.2. The results are compared with the results obtained from the analysis of the integrated momentum equation from section 2.2. Comparison with other DNS and experiments is also made. In section 4.3, turbulent statistics are presented and results obtained from the equations describing the inner part of the turbulent boundary layer are compared with the statistics from the DNS. In the last section 4.4, results using

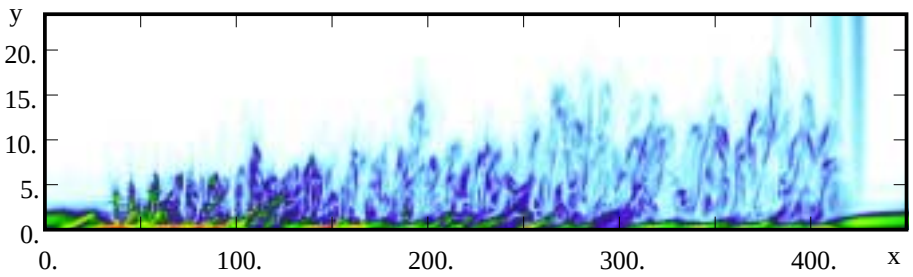

FIGURE 3. APG2: Contours of vorticity.

the differential Reynolds stress model are compared with the low Reynolds number DNS data. The model predictions are also extended to high Reynolds numbers to determine the asymptotic behavior.

4.1. *Flow structures*

Figure 3 shows an instantaneous vorticity flow field from the APG2 case. At $x = 0$ the boundary layer is laminar and at $x = 10$ the stochastic volume force triggers transition. The transition to turbulence is rapid and at approximately $x = 150$ the turbulent flow has become fully developed. In the turbulent region, shear layers inclined in the downstream direction can be seen as red and yellow contours. They indicate the presence of turbulent 'bursts' in the near wall region. In the outer part of the boundary layer larger scale vortical structures can be seen. Note the 'fringe region' at the end of the computational box, starting at $x = 400$.

The streamwise velocity fluctuations close to the wall in Figure 4 show the dominance of streamwise aligned streaks. The speed of the low speed streaks is about 0.16 and 0.29 for the high speed streaks at the position of $y^+ = 10$. The spacing of the low speed streaks is about 100 plus-units. These values are about the same as those found in zero pressure gradient turbulent boundary layers, see Figure 5 for comparison. If the whole field in the normal direction is shown at a value of $x = 280$ as in Figure 6, a second layer of 'streaks' is found at $y = 3.5 - 8$.

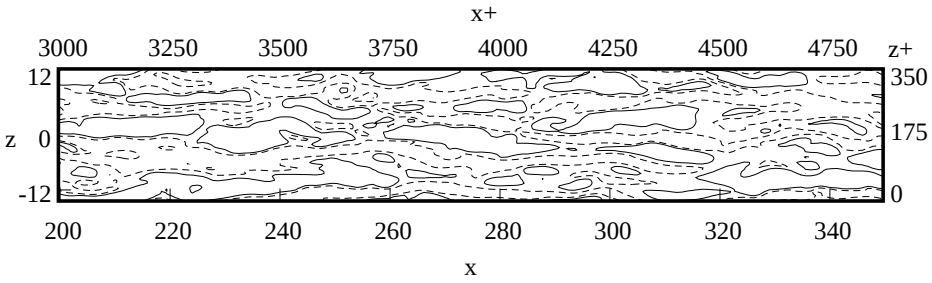

FIGURE 4. APG2: Streamwise velocity fluctuation in a plane $y = 0.7$ or $y^+ = 10$, contours at -0.05 (dashed) and 0.05.

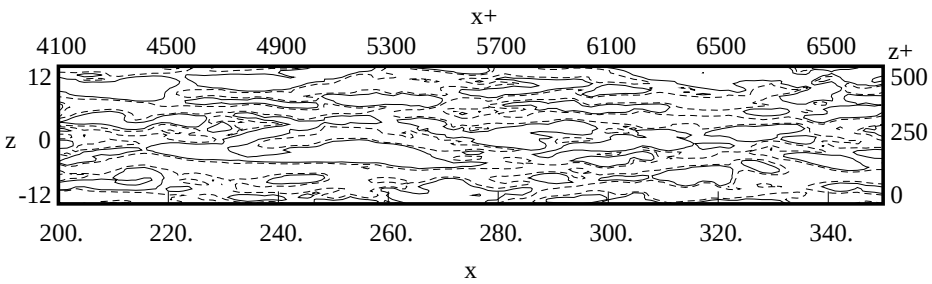

FIGURE 5. ZPG: Streamwise velocity fluctuation in a plane $y = 0.5$ or $y^+ = 10$, contours at -0.05 (dashed) and 0.05.

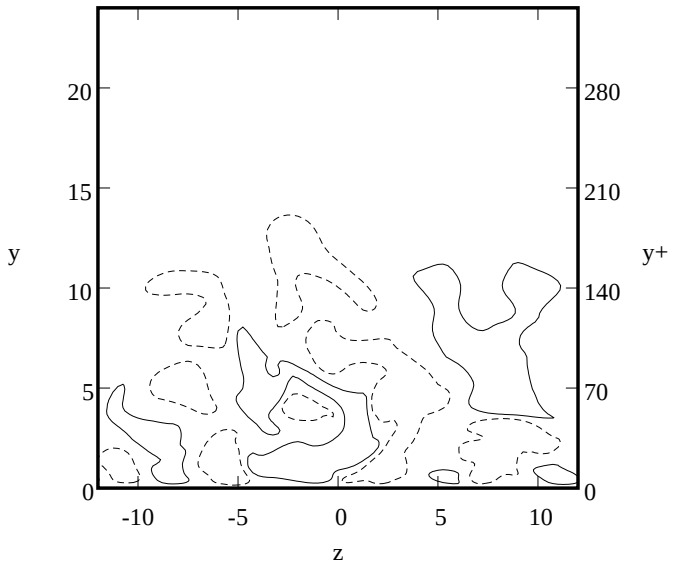

FIGURE 6. APG2: Streamwise velocity fluctuation in a plane $x = 280$, contours at -0.05 (dashed) and 0.05.

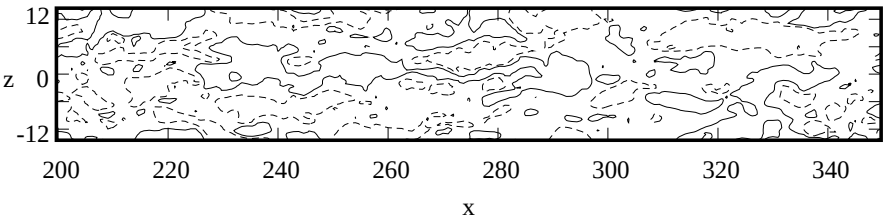

FIGURE 7. APG2: Streamwise velocity fluctuation in a plane $y = 4$ or $\eta = 0.6$, contours at -0.05 (dashed) and 0.05.

If plotted in a plane at $y = 4$ (Figure 7) it can be seen that the streaky structures in the outer part of the boundary layer are shorter and wider compared to the ones closer to the wall. The upper streaks are also present in the zero pressure gradient case and are not a consequence of the adverse pressure gradient, but they are intensified by the pressure gradient and can be related to the outer maximum observed in the turbulent kinetic energy and turbulent production. This observation is further discussed in section 4.3.2. Comparing Figures 4 and 5 the streaks close to the wall also become shorter for stronger adverse pressure gradients. In the DNS of Spalart & Leonard (1987) for a turbulent boundary layer near separation the streaks have become so thick and short that they are instead aligned in the spanwise direction. A part of the computational box is shown in Figure 8 for the APG2 case. The color bar indicates the streamwise disturbance velocity. The contour plots are at the blue level of -0.08. Notice the long streaks close to the wall and the shorter streaks located in the upper part of the boundary layer.

4.2. *Mean flow characteristics*

4.2.1. *Self-similarity*

The β-parameter is shown for the two APG cases in Figure 9a, and H as a function of Re_Θ for all three cases in Figure 9b. The β-parameter is close to constant and the shape factor varies slowly, particularly for the higher adverse pressure gradient. As seen in Figure 10 the Clauser parameter, G (equation 17), is about 7.6 for APG1 and varies between 8.0 and 8.3 for APG2 (further discussed in section 4.4.1). Thus we can conclude that the simulations fulfill the requirements for self-similarity reasonably well. In Figure 11 the skin friction, C_f, is shown together with the freestream velocity. C_f is lower for higher pressure gradients and would become zero at separation. Note that the figures showing β and C_f include the small laminar state and the transitional region.

The velocity profiles from the two present simulations are compared with Spalart's ZPG case (Spalart 1988) at almost the same Reynolds number $Re_\Theta = 670$ in Figure 12. There is a small shift downward of the logarithmic part, but

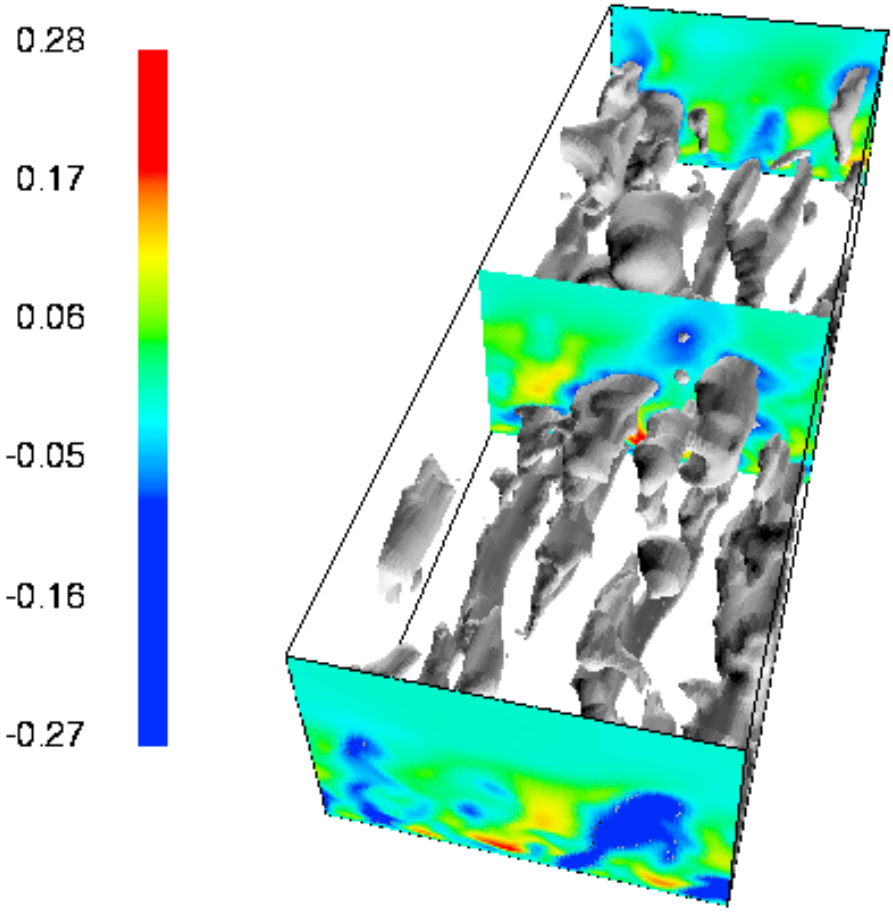

FIGURE 8. APG2: Streamwise velocity fluctuations. The color bar indicates the streamwise disturbance velocity. The level of the contour plot is -0.08. The streamwise direction is upward in the figure. The extension of the box is x=246—319, y=0—15, z=-12—12.

the log-region is too small to draw any conclusions about the effect of the adverse pressure gradient on the log-law.

As the β-parameter is constant we might expect a self-similar boundary layer. From the velocity profiles in the outer scaling at positions downstream (Figure 13b), it is difficult to draw any conclusions about self-similarity in the outer part of the boundary layer since the Reynolds number variation is small. In the inner scaling, the self-similarity is very clear since the velocity profiles collapse in the inner part as seen in Figure 13a.

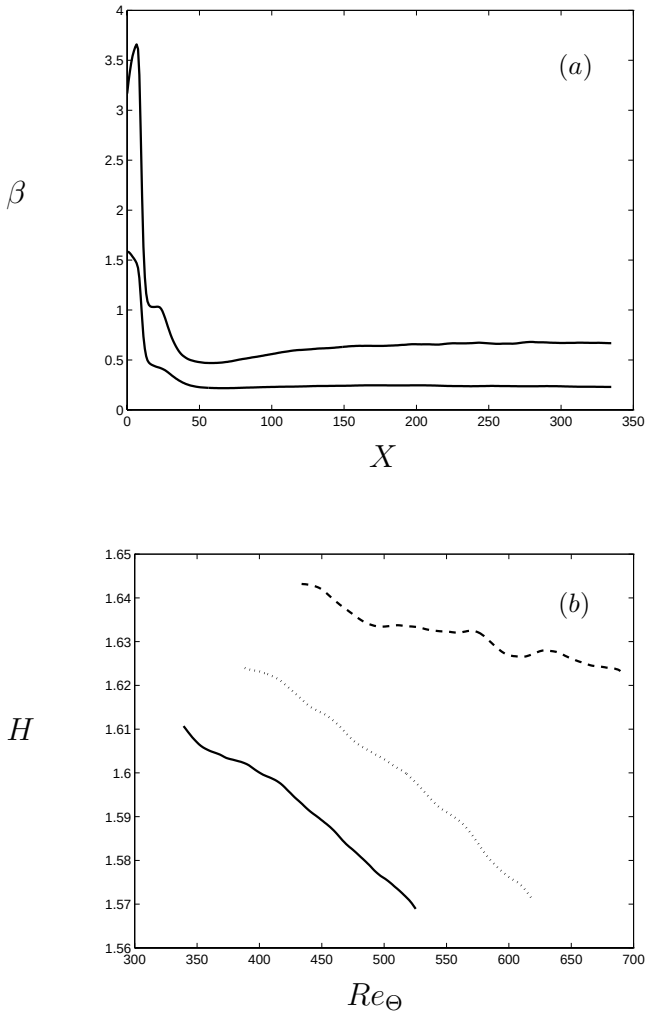

FIGURE 9. (a) β for the two APG cases. (b) H. — ZPG; $\cdots$ APG1; - - APG2.

4.2.2. *Separation prediction*

In Table 2 we have compiled data from the present simulations, together with data from existing experiments and numerical simulations. The relationship between β and m obtained from the linear, equation (13), and non-linear, equation (27), theories are evaluated. The overall conclusion from the table is that the relation from the non-linear analysis is in much better agreement with the measured and simulated cases than the linearized relation. It should be noted that the considered cases have widely different Reynolds numbers.

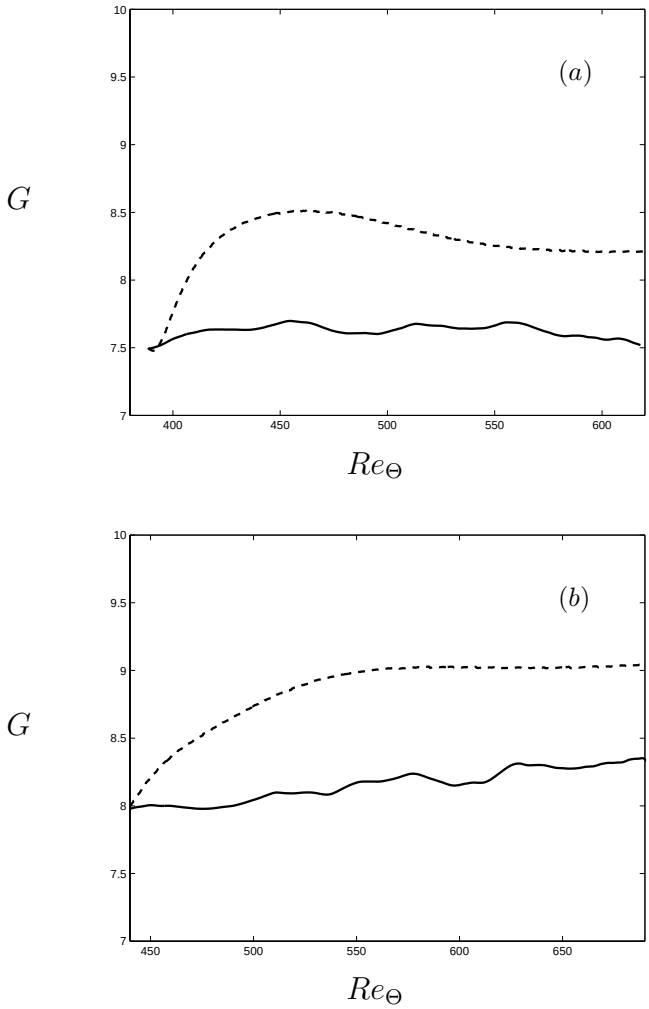

FIGURE 10. (a) G for APG1. (b) G for APG2. — DNS; - - DRSM.

The first two cases are the simulations presented here. The non-linear relation is in better agreement for the stronger pressure gradient (APG2). This might be explained from Figure 9b where the shape factor is closer to a constant in APG2 than APG1. Bradshaw's two measurements (Bradshaw 1967) are shown next, where a better agreement is obtained for the stronger pressure gradient. Skåre & Krogstad (1994) performed experiments on turbulent boundary layers near separation. The agreement with the non-linear relation is excellent while the linear counterpart does not agree. We also see that the shape factor is about two and not one as the linear analysis requires. The data from the measurements by Stratford (1959*a*) of a turbulent boundary layer near

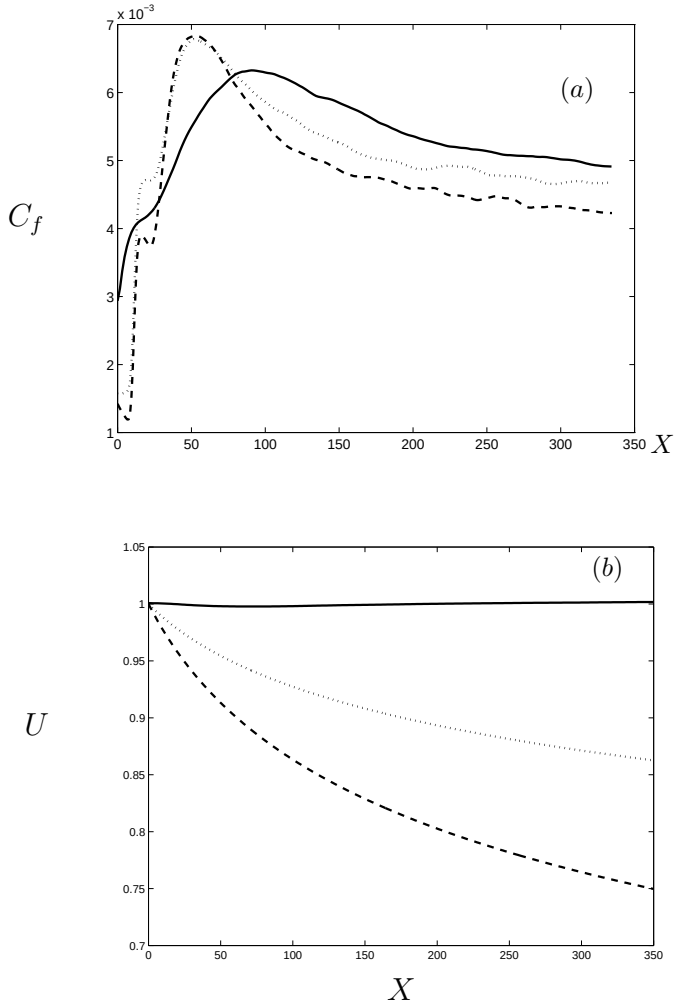

FIGURE 11. (a) C_f. (b) U. — ZPG; $\cdots$ APG1; - - APG2.

separation lead to the same conclusions as the previous case. The last five cases are from the DNS of Spalart & Leonard (1987). The agreement is good for all these cases, the first two are equivalent to the measurements by Clauser (1954), and the third one is near separation. These simulations were performed using a similarity coordinate system which permitted temporal simulations of spatially developing boundary layer. They also performed simulations of Bradshaw's two cases by using the same value of β. The first case corresponds closely to our APG2. The Reynolds number based on the displacement thickness is the same in their simulation as at the end of our spatial simulation. Their value of the shape factor is lower than ours, and m is more negative.

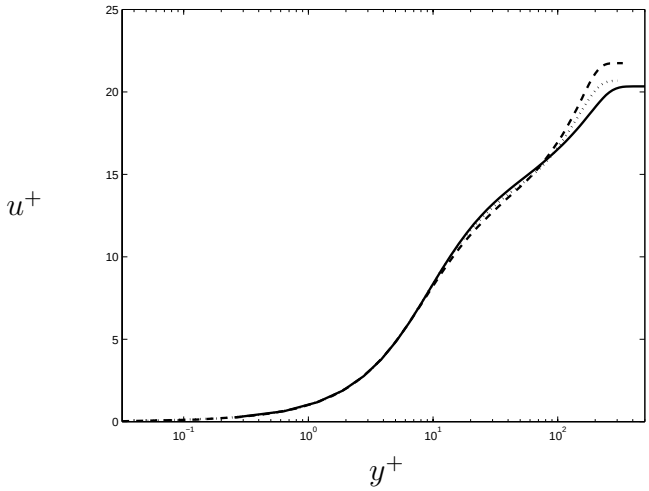

FIGURE 12. Velocity profiles in the inner scaling for — Spalart; $\cdots$ APG1; - - APG2.

Case	β	H	m	$m = -\frac{\beta}{H(1+\beta)+2\beta}$	$m = -\frac{\beta}{1+3\beta}$
APG1	0.24	1.60	-0.077	-0.097	-0.14
APG2	0.65	1.63	-0.15	-0.16	-0.22
Bradshaw 1	0.9	1.4	-0.15	-0.20	-0.24
Bradshaw 2	5.4	1.54	-0.255	-0.26	-0.31
Skåre & Krogstad	20.0	2.0	-0.22	-0.24	-0.33
Stratford	∞	2.5	-0.23	-0.22	-0.33
Spalart & Leonard	1.8	1.65	-0.21	-0.22	-0.28
	8.0	1.92	-0.23	-0.24	-0.32
	∞	2.3	-0.22	-0.23	-0.33
	0.9	1.55	-0.18	-0.19	-0.24
	5.4	1.86	-0.24	-0.24	-0.31

TABLE 2. Comparison of m from the non-linear/linear theory.

Using the linearized relation (13) gives a value of the parameter $m = -0.33$ for all three investigations of near separation in Table 2. The non-linear relation (27) reduces to $m = -1/(H + 2)$, which gives much more realistic values of m since the shape factor in the experiments is far from its asymptotic value of one in the near separation cases.

The conclusion from this comparison is that the approximation $u_\tau/U =$ const. can be used successfully if one is interested in obtaining relations between mean flow parameters at low and moderate Reynolds numbers. Even though the Reynolds number in experiments is high enough to get self-similarity, the

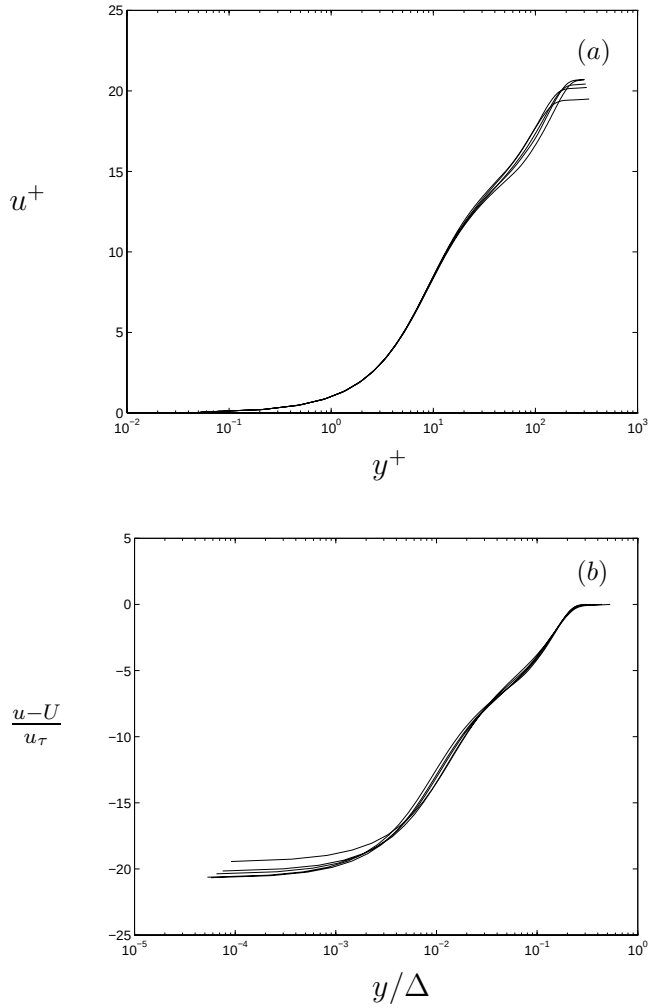

FIGURE 13. APG1: Velocity profiles for five positions downstream, starting at $x = 150$ with an increment of 50, ending at $x = 350$. (a) Inner scaling. (b) Outer scaling.

slow variation of H and thus u_τ/U makes the approximation $u_\tau/U \to 0$ unsuitable as a starting point for the analysis of the equations. This slow variation is also evident in the calculations with turbulence models, which will be described later.

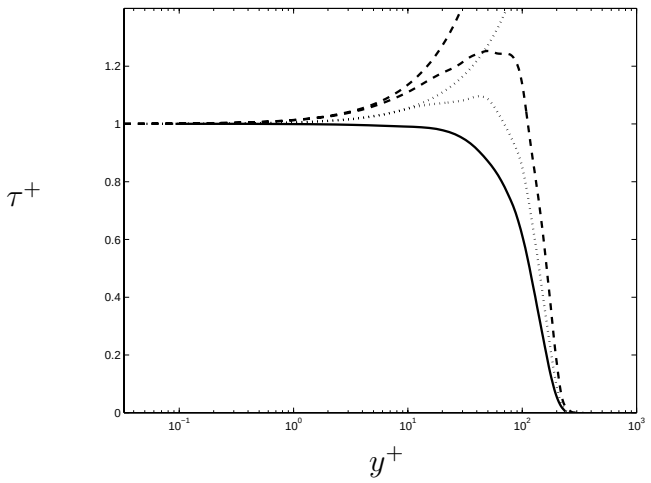

FIGURE 14. Shear stress. — ZPG; ··· APG1; - - APG2. Shear stress evaluated from equation (40) diverges, whereas the total shear stress from DNS approaches zero for large y^+.

4.3. *Higher order statistics*

4.3.1. *Scalings in the inner part of the boundary layer*

The equations governing the inner part of an adverse pressure gradient boundary layer are the continuity equation (1) and the momentum equation (2) with the non-linear, advective terms neglected, i.e.

$$0 = -\frac{1}{\rho}\frac{dP}{dx} + \nu\frac{\partial^2 u}{\partial y^2} - \frac{\partial}{\partial y}\langle u'v'\rangle. \tag{37}$$

When using the inner length and velocity scales ν/u_τ and u_τ respectively, equation (37) can be written as

$$0 = -\frac{\beta}{Re_*} + \frac{\partial^2 u^+}{\partial y^{+^2}} - \frac{\partial}{\partial y^+}\langle u'v'\rangle^+, \tag{38}$$

where $Re_* = (u_\tau \delta^*)/\nu$. If the ratio β/Re_* is smaller than the other terms, the equation reduces to the same one that governs the inner part of a ZPG boundary layer. However, for APG cases at low Reynolds numbers or close to separation this term cannot be neglected. Equation (38) can be written as

$$\frac{\partial}{\partial y^+}\left(\frac{\partial u^+}{\partial y^+} - \langle u'v'\rangle^+\right) = \frac{\beta}{Re_*} = \frac{\nu}{u_\tau^3}\frac{1}{\rho}\frac{dP}{dx} \tag{39}$$

and after integration, one finds the following expression for the total shear stress

$$\tau^+ \equiv \frac{\partial u^+}{\partial y^+} - \langle u'v'\rangle^+ = 1 + \frac{\nu}{u_\tau^3}\frac{1}{\rho}\frac{dP}{dx}y^+. \tag{40}$$

The total shear stress, τ^+, from the DNS and the curves $\tau^+(y^+)$ represented by equation (40) are shown in Figure 14. The term

$$\frac{\beta}{Re_*} = \frac{\nu}{u_\tau^3}\frac{1}{\rho}\frac{dP}{dx} \tag{41}$$

is evidently important for the shear stress distribution in the inner part of the boundary layer at low Reynolds numbers. If we define a new velocity scale,

$$u_p = \left(\nu\frac{1}{\rho}\frac{dP}{dx}\right)^{1/3}, \tag{42}$$

the term (41) can be written as

$$\frac{\beta}{Re_*} = \left(\frac{u_p}{u_\tau}\right)^3. \tag{43}$$

One might expect that it is the magnitude of the ratio between the two velocity scales u_p and u_τ that determines which one to use in the scaling of equation (37). If u_p and ν/u_p are used as the velocity and length scales respectively, the integrated version of equation (37) becomes

$$\frac{\partial u^p}{\partial y^p} - \langle u'v'\rangle^p = y^p + \left(\frac{u_\tau}{u_p}\right)^2. \tag{44}$$

If $u_\tau \ll u_p$, i.e. the boundary layer is close to separation, the scalings based on u_p should be used, but for the APG cases considered here, u_τ is the proper scaling, which is evident from Figure 13a, where the velocity profiles for downstream positions are shown. The profiles collapse on the curve $u^+ = y^+$ in the viscous sub-layer, which is consistent with equation (40), which reduces to

$$\frac{\partial u^+}{\partial y^+} = 1 \tag{45}$$

when $y^+ \to 0$.

When multiplying equation (40) by $\partial u^+/\partial y^+$ we get the mean energy budget.

$$\left(\frac{\partial u^+}{\partial y^+}\right)^2 - \langle u'v'\rangle^+\frac{\partial u^+}{\partial y^+} = \frac{\partial u^+}{\partial y^+} + \frac{\beta}{Re_*}y^+\frac{\partial u^+}{\partial y^+}. \tag{46}$$

The same equation is obtained if equation (38) is multiplied by u^+. The terms are noted from left to right: direct dissipation, production, transport and pressure gradient term. The mean budget for the APG2 case in the inner region is shown in Figure 15a. The largest contribution in the near wall region comes from the direct dissipation which is balanced by the transport term. At $y^+ = 5$ the pressure gradient term has reached its maximum and then stays constant. The production of turbulent energy has its maximum at $y^+ = 9$ where the production and direct dissipation are equal in magnitude. All the terms balance each other, though the total sum deviates from zero at large values of y^+. If the advective terms also are included in the total budget, the sum becomes zero but these terms are small compared to the others.

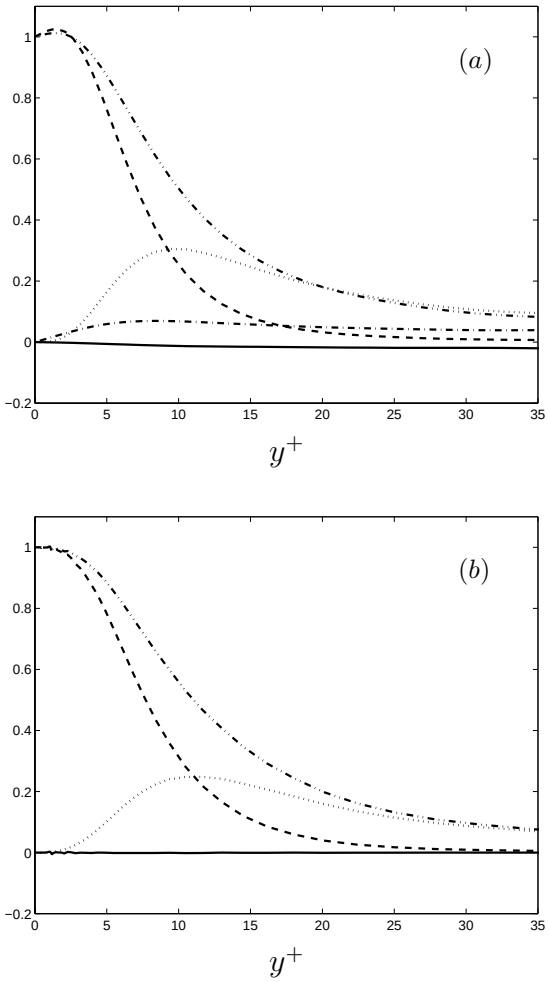

FIGURE 15. Energy budget for DNS: - - Dissipation; $\cdots$ Production; - $\cdots$ - Transport; - $\cdot$ - Pressure gradient term; — Total. (a) DNS. (b) DRSM, asymptotic.

The same energy budget but for the DRSM prediction is almost identical. More interesting is to look at the budget for the high Reynolds number case, which is shown in Figure 15b. Here the pressure gradient term has vanished from the budget. This is due to the term $1/Re_*$ in the pressure gradient term in equation (46). The sum of the terms is zero which implies that the advective terms no longer has any influence on the inner layer.

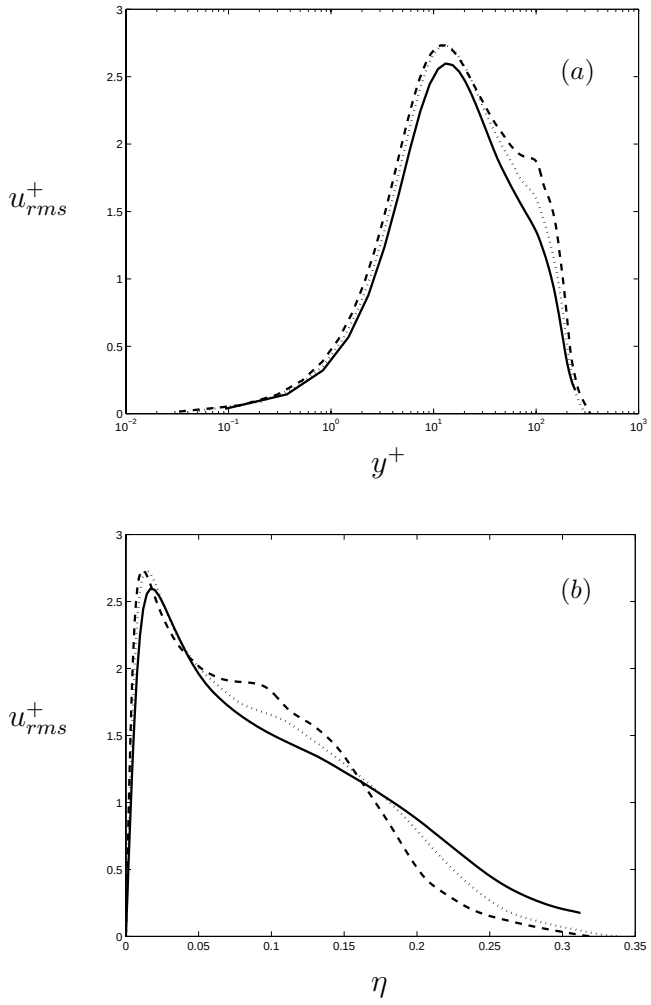

FIGURE 16. u^+_{rms} at $x = 300$. — ZPG; $\cdots$ APG1; - - APG2. (a) Inner scaling. (b) Outer scaling.

4.3.2. *The Reynolds stresses and turbulent production*

In Figure 16 u_{rms} for the ZPG/APG cases are shown in inner and outer scaling for the same streamwise station. There is only a slight difference between the cases in the inner region but in the outer region the tendency towards a second peak in the u_{rms} profile for the highest pressure gradient marks a clear difference. This outer maximum has been observed in a number of experimental studies, such as Bradshaw (1967), Samuel & Joubert (1974), Nagano *et al.* (1992) and Skåre & Krogstad (1994). The production term in the turbulent energy budget also has an outer peak for the higher pressure gradient case, as

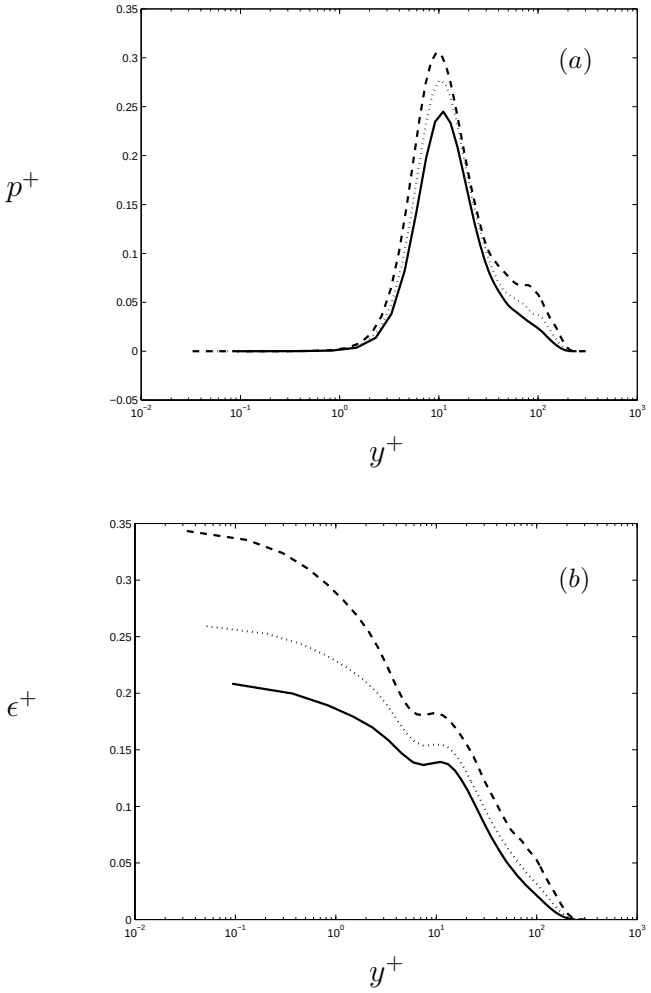

FIGURE 17. (a) Production at $x = 300$. (b) Dissipation at $x = 300$. — ZPG; $\cdots$ APG1; - - APG2.

seen in Figure 17a. These outer peaks in the turbulent energy and production might be related to the enhanced streak formation in the outer part of the boundary described in section 4.1. There are no outer peaks in the v_{rms} and w_{rms} profiles.

The location of the inner maximum of the production can be motivated by the form of the near-wall limit of the turbulent boundary layer equations. The integrated inner equation for the ZPG case can be written as

$$-\langle u'v'\rangle^+ = 1 - \frac{\partial u^+}{\partial y^+}. \tag{47}$$

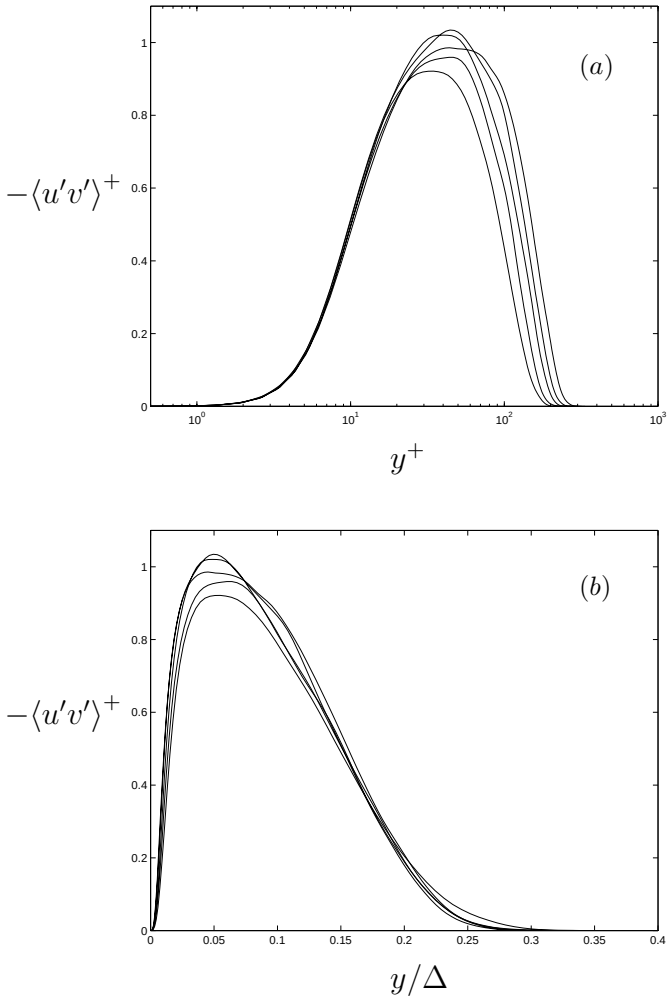

FIGURE 18. APG1: Reynolds shear stress profiles for five positions downstream, starting at $x = 150$ with an increment of 50, ending at $x = 350$. (a) Inner scaling. (b) Outer scaling.

When used in the expression for the turbulent production

$$p^+ = -\langle u'v'\rangle^+ \frac{\partial u^+}{\partial y^+}, \tag{48}$$

this yields

$$p^+ = \left(1 - \frac{\partial u^+}{\partial y^+}\right) \frac{\partial u^+}{\partial y^+}. \tag{49}$$

p^+ has a maximum of 0.25 at the position where $\partial u^+/\partial y^+ = 0.5$. The inner maximum is increased due to the pressure gradient but the position is not changed as can be seen in Figure 17a.

The dissipation is shown in Figure 17b, where an increased dissipation for higher pressure gradients is observed near the wall.

The profiles for the Reynolds stress in the outer scaling (Figure 18b) show that self-similarity is not yet obtained since the maximum grows downstream. In the inner scaling the profiles collapse as seen in Figure 18a. This non-similarity in the outer part is due to low Reynolds number, as will be more clearly understood when a comparison with model predictions is made in the next section, where also the higher order statistics from the DNS will be considered.

4.4. *Comparison with turbulence model predictions*

Henkes (1998) has tested some turbulence models for high Reynolds number self-similar APG turbulent boundary layers at high Reynolds number. All the tested models, $k-\epsilon$, $k-\omega$ and differential Reynolds stress models, give results that approach the same asymptotic scalings for the velocity and the Reynolds shear stress. However, differences occur in the scaled similarity profiles, as well as in parameters like H, G and C_f. When comparing with available experiments at moderate Reynolds numbers, the differential Reynolds stress model turns out to be superior to the others. Here we will use the Differential Reynolds Stress Model (DRSM) of Hanjalić *et al.* (1995) described in section 3.3 for both the high and low Reynolds number predictions.

4.4.1. *Low Reynolds number*

In this section calculations with the DRSM performed at low Reynolds numbers for comparison with data from our DNS (Henkes *et al.* 1997) are presented. Mean turbulent profiles for the velocities, Reynolds stresses and the dissipation from the DNS at $x = 150$ were used as initial data. Comparison was made at $x = 350$ for APG1 and $x = 335$ for APG2. At these positions the Re_Θ is approximately 620 for APG1 and 690 for APG2. The DRSM calculations show that transients are dominating in the beginning of the calculations but at the point of comparison with the DNS-data the solution is not sensitive to small changes in initial data. It was also checked that changes in the length and velocity scales of the initial data did not affect the solution at the point of comparison. Thus the comparison is meaningful since the difference between the model predictions at low and high Reynolds number are due to the dependence on the Reynolds number and not to the influence of the initial conditions.

The shape factor is shown in Figures 19a and 19b for APG1 and APG2. After the decay of the initial transients the Reynolds number dependence of the shape factor is captured by the model, although there is a slight offset in the numerical values. The comparison of the Clauser parameter G for the DNS and DRSM is shown in Figures 10a and 10b. As in the case of the shape

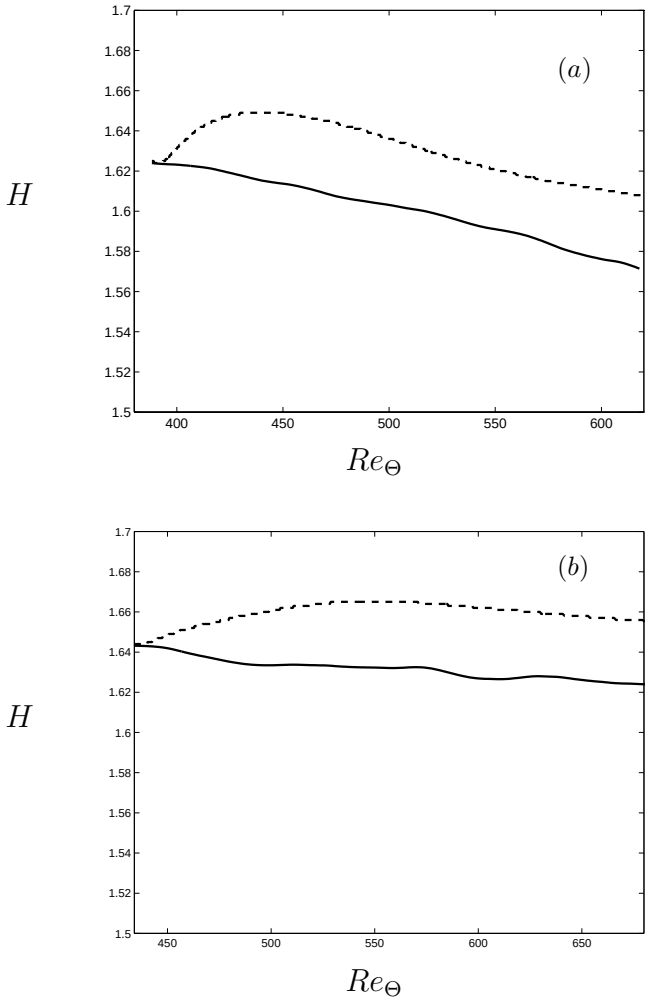

FIGURE 19. (a) H for APG1. (b) H for APG2. — DNS; - - DRSM.

factor, the Reynolds number dependence is captured after the decay of the initial transients. The profiles for the mean velocity, the Reynolds stress and u_{rms} from the model predictions are compared with the DNS data in Figures 20 to 22. Only the APG2 case is shown since here the differences between DNS and DRSM are larger than for the APG1 case. The self-similar high Reynolds number profiles according to the DRSM are also shown in these figures for comparison, but will be discussed more thoroughly in the next section.

In Figures 20a and 20b the mean velocity profiles from the DNS and DRSM are shown together with the self-similar high Reynolds number profile. At the point of comparison, only a small logarithmic part in the inner layer is found as

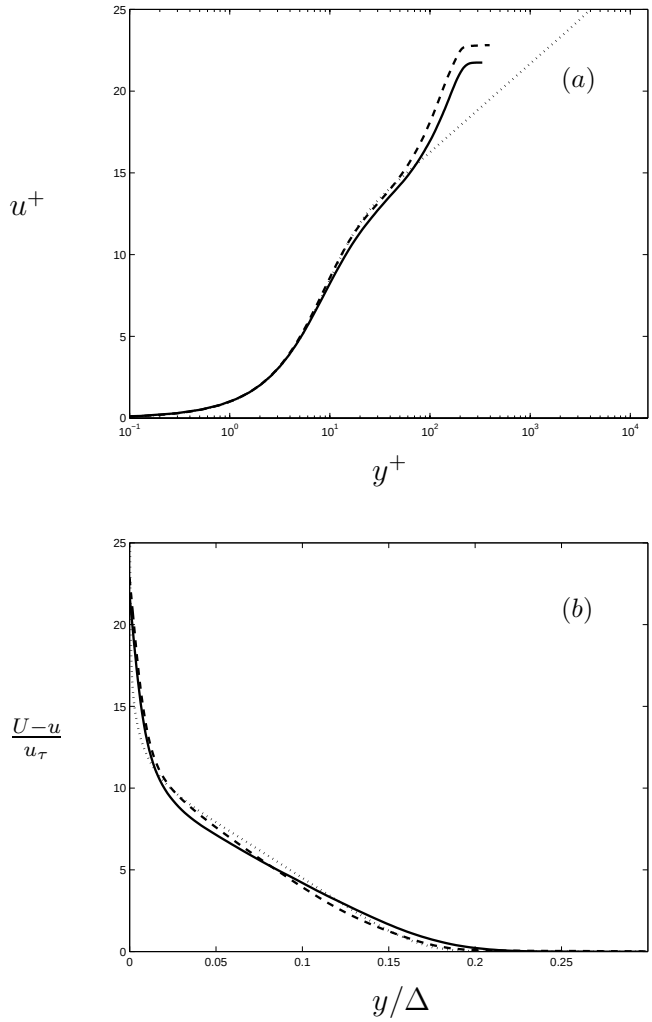

FIGURE 20. Velocity profiles for APG2. — DNS; - - DRSM; ··· Asymptotic. (a) Inner scaling. (b) Outer scaling.

seen in Figure 20a. The agreement between the DRSM and DNS in the inner part is excellent. The velocity profiles in the outer scaling do not show very large differences between the DNS, DRSM and the asymptotic DRSM profile as seen in Figure 20b. The Reynolds stress profiles in the inner and outer scalings are shown in Figures 21a and 21b. In the near wall region, the DRSM profile is in close agreement with DNS and the deviation from the asymptotic profile is well captured by the model. The plateau value of 1 seen in the asymptotic profile has not yet been developed. The peak in the profiles belongs to the outer part of the boundary layer as seen in Figure 21b and is larger in the asymptotic

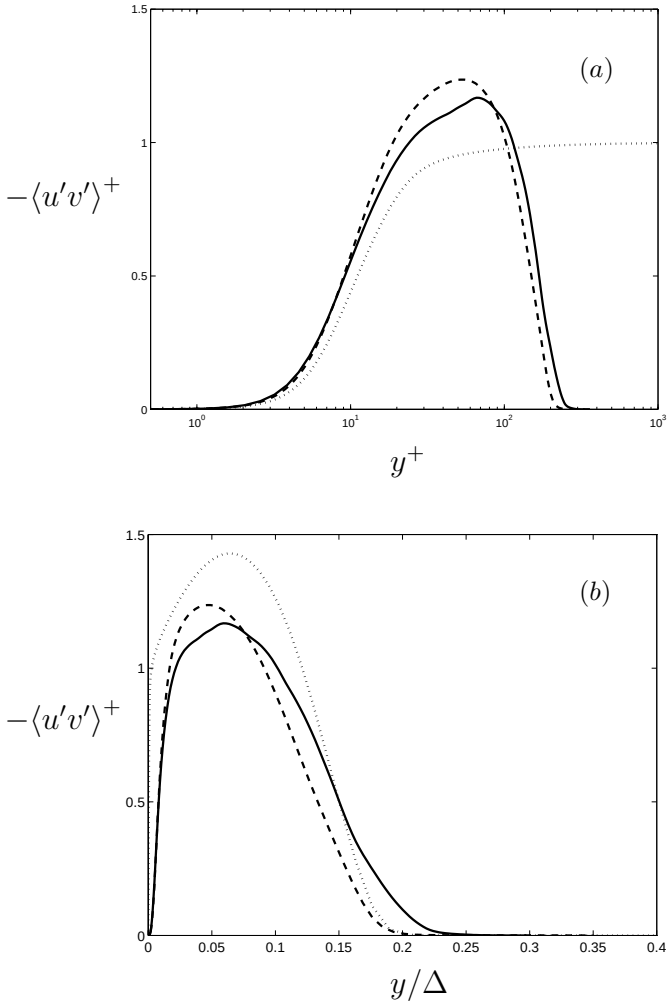

FIGURE 21. Reynolds stress for APG2.— DNS; - - DRSM; ··· Asymptotic. a) Inner scaling. b) Outer scaling.

profile. Figure 21b also reveals that the DRSM gives a profile below the DNS in the outer part of the boundary layer. The u_{rms} profiles in the inner and outer scalings are shown in Figures 22a and 22b. In the near wall region region, the profile from the DRSM is closer to the asymptotic profile than the DNS profile. The inner peak value in the asymptotic profile is lower than the peaks in the low-Re profiles. In the outer scaling, shown in Figure 22b, the DRSM profile is below the DNS profile in the same way as for the Reynolds stress profiles. The outer peak seen in the low-Re profiles is still relatively far from its value in the asymptotic DRSM profile. By comparing the inner and outer peaks in

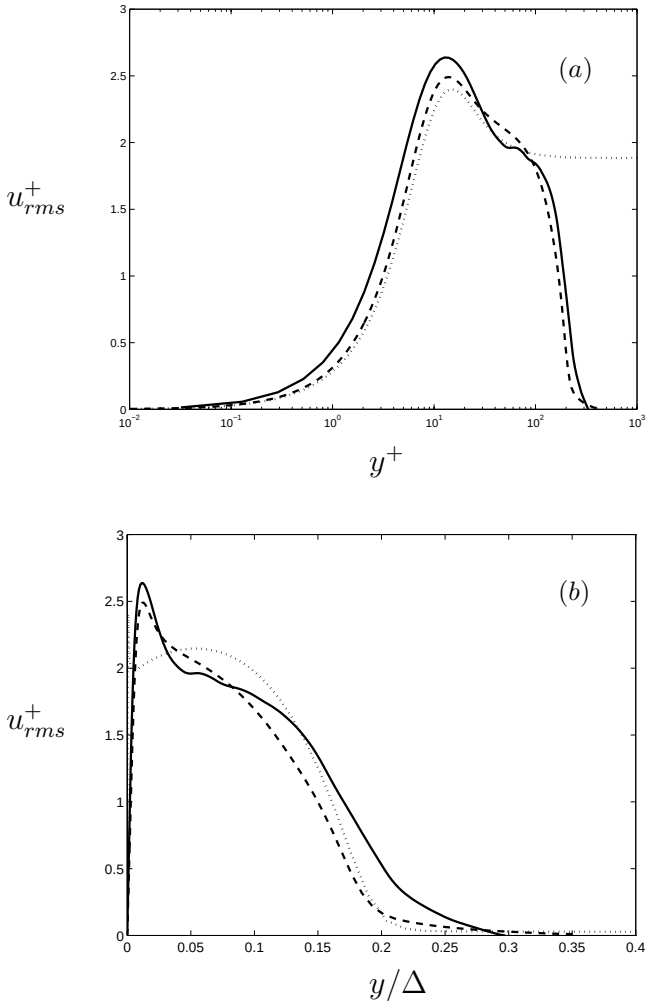

FIGURE 22. u^+_{rms} for APG2. — DNS; - - DRSM; $\cdots$ Asymptotic. a) Inner scaling. b) Outer scaling.

the u_{rms} profiles, we may conclude that turbulent energy is transfered from the inner part to the outer part of the boundary layer when the self-similar state is approached.

These results show that although differences between the DRSM solution at $Re_\theta = 690$ and the similarity solution are significant, the results with the DRSM closely agree with the DNS at $Re_\Theta = 690$. This suggests that the DRSM reproduces the physics of adverse pressure gradient boundary layers at relatively low Reynolds numbers.

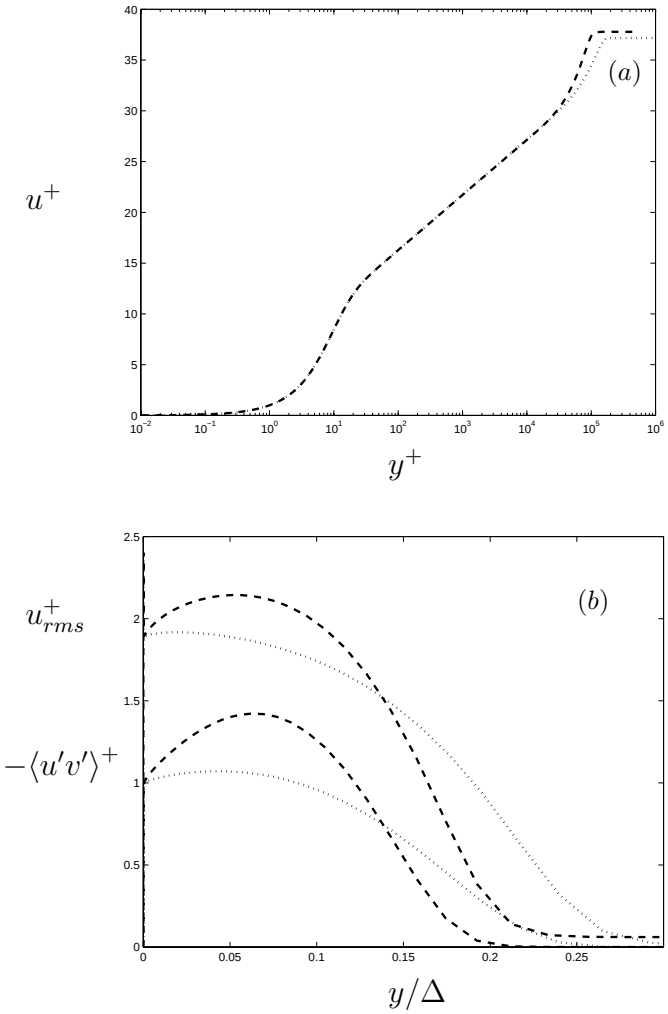

FIGURE 23. High Reynolds number profiles: a) Velocity defect. b) u^+_{rms} and $-\langle u'v' \rangle^+$. $\cdots$ APG1; - - APG2.

4.4.2. *High Reynolds number*

DRSM predictions of the two adverse pressure gradients cases, APG1 and APG2, were started at the same Reynolds number at which the DNS was performed and then continued up to very high Reynolds number. Above Re_Θ of about 10^4 the velocity and Reynolds stress profiles in the outer scaling are self-similar.

The self-similar velocity profiles in the inner scaling, (Figure 23a), show that the slope of the asymptotic profile, i.e. the Kármán constant, does not

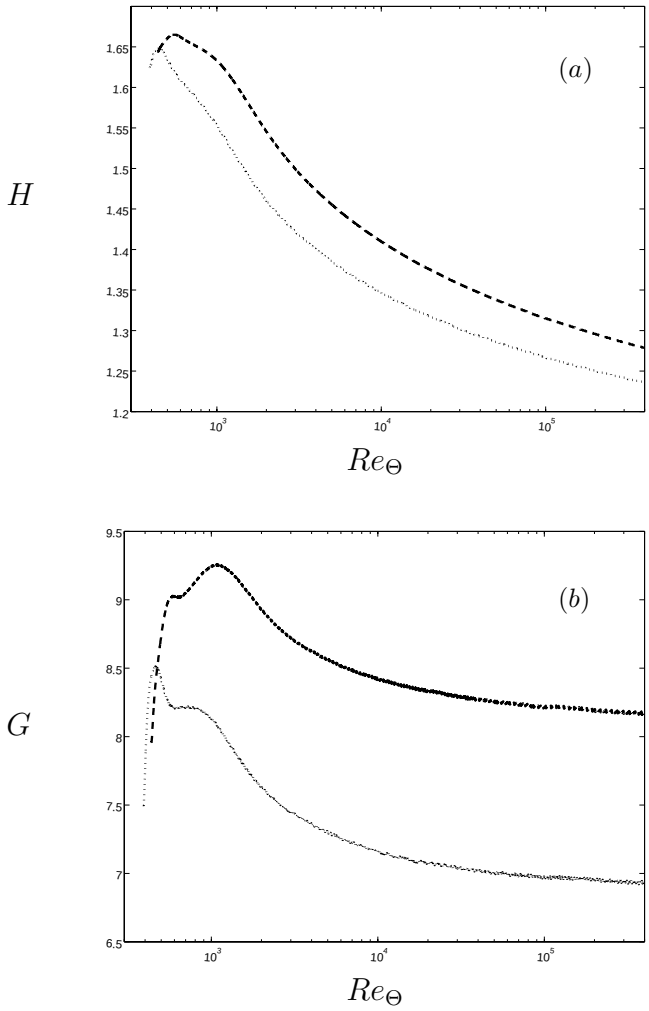

FIGURE 24. a) H. b) G. $\cdots$ APG1; - - APG2.

change with the pressure gradient. In Figure 23b the self-similar Reynolds stress and u_{rms} profiles are shown in the outer scaling. The peaks in the profiles are the outer ones. The inner peak of the u_{rms} and the plateau value of 1 for the Reynolds shear stress are not visible in the outer scaling. Compare with the Figures 21 and 22 where the asymptotic profiles are shown in both the inner and outer scalings. It is only for the APG2 case that the outer peak in the u_{rms} profile appears. Apparently the adverse pressure gradient in APG1 is too weak for an outer peak to develop. The asymptotic behavior of H and G are shown in Figures 24a and 24b. H should approach 1 and G a constant value at infinite Re. The figures show that the asymptotic values and therefore complete

self-similarity are far from being reached although the Reynolds number is very large. The values are further from the asymptotic values for APG2 than for APG1.

From the mean velocity and Reynolds stress profiles one might conclude that self-similarity is obtained, but the downstream variation of H and G show that the asymptotic state of the flow is very slowly approached. In the experiments by Skåre & Krogstad (1994) the results were interpreted as self-similarity although the constant shape factor was far from the asymptotic value. These experiments were performed at Re_Θ between 10^4 and 10^5, and the results can be explained by the high Reynolds number behavior of the velocity profile and the shape factor which appear to be constant if the Reynolds number is not varied enough. The slow variation of mean flow parameters was also utilized to derive the mean flow relations in section 2.2.

5. Summary and Conclusions

DNS of the Navier-Stokes equations has been carried out with the objective of studying APG turbulent boundary layers. The pressure gradient parameter is found to be constant when the freestream velocity varies according to a power law, which has also been shown to follow from the turbulent boundary layer equations. To relate the exponent in the power law to the pressure gradient parameter, an analysis based on the assumption of asymptotically high Reynolds number was first reviewed. The assumption implies that the ratio of the friction velocity to the freestream velocity is zero. This is obtained from the logarithmic friction law and the matching of inner and outer solution of the mean turbulent boundary layer equations. Another consequence of the assumption is that the shape factor becomes one, which is equivalent to a linearization of the velocity defect. The mean turbulent flow was investigated with a differential Reynolds stress model for high Reynolds numbers. These investigations showed that even at very high Reynolds number the asymptotic value for the shape factor is still far from being obtained although a self-similar state of the velocity and Reynolds shear stress profiles has been reached. This is also evident from a number of experiments and can also be related to the fact that the logarithmic function increases slowly when the argument is large. These observations motivated a different approach to the analysis of the mean turbulent boundary layer equations.

A non-linear analysis of the equations describing the mean flow based on the approximation of a constant ratio of the freestream velocity to the friction velocity was presented. The analysis leads to a relation for the power law, in which both the pressure gradient parameter and the shape factor appear. This relation gives better agreement with available numerical and physical experiments than the linearized analysis. It was shown that the agreement is better over a range of different Reynolds numbers, particularly regarding the parameters for which separation occurs. The relation from the linearized, asymptotic

analysis is recovered from the new relation obtained from the less restricted analysis by letting the shape factor become one.

Comparison of turbulent statistics from the ZPG and the two APG cases shows the development of a second peak in the turbulent energy in agreement with experiment. The analysis of the inner equations and investigation of the behavior of the total shear stress showed that the pressure gradient parameter is also important in the inner layer at the low Reynolds number flows performed with DNS. The Reynolds shear stress profiles showed no self-similar state although the pressure gradient parameter was constant. This is due to low Reynolds number effects and motivated the use of model predictions to first try to reproduce the low Reynolds number effects and then increase the Reynolds number as to obtain the self-similar state.

The differential Reynolds stress model was used to predict the mean flow at the same low Reynolds number as the DNS. Initial data for the model predictions were taken from the DNS at the lowest Reynolds number where fully developed turbulence was obtained. After the decay of some small initial transients the Reynolds number dependence of mean flow parameters such as the shape factor and Clauser parameter, was captured by the model. Comparison with data from DNS at the highest Reynolds number obtained, showed that low Reynolds number effects are well captured by the model. The model predictions could be continued up to high Reynolds numbers to obtain self-similarity. By comparing the profiles at low and high Reynolds numbers, the lack of self-similarity in the Reynolds stress profiles in the DNS could thus be attributed to effects of low Reynolds number.

Acknowledgments

This work was sponsored by the Swedish National Board for Industrial and Technical Development (NUTEK).

Appendix A.

The two-dimensional boundary layer equations for the Differential Reynolds Stress Model of Hanjalić *et al.* (1995) are:

Conservation of mass:

$$\frac{\partial u}{\partial x} + \frac{\partial v}{\partial y} = 0. \tag{50}$$

Conservation of momentum:

$$u\frac{\partial u}{\partial x} + v\frac{\partial u}{\partial y} = -\frac{1}{\rho}\frac{dP}{dx} + \nu\frac{\partial^2 u}{\partial y^2} - \frac{\partial}{\partial y}\langle u'v'\rangle. \tag{51}$$

Equation for the Reynolds shear stress:

$$u\frac{\partial\langle u'v'\rangle}{\partial x}+v\frac{\partial\langle u'v'\rangle}{\partial y}=\frac{\partial}{\partial y}\left[\left(\nu+C_s\frac{k}{\epsilon}\langle v'^2\rangle\right)\frac{\partial\langle u'v'\rangle}{\partial y}\right]+P_{12}+\Phi_{12}-\epsilon_{12}, \quad (52)$$

with

$$P_{12}=-\langle v'^2\rangle\frac{\partial u}{\partial y},$$

$$\Phi_{12}=-\left(C_1+\frac{3}{2}C_1^w f_w\right)\frac{\epsilon}{k}\langle u'v'\rangle+\left(1-\frac{3}{2}C_2^w f_w\right)C_2\langle v'^2\rangle\frac{\partial u}{\partial y},$$

$$\epsilon_{12}=\epsilon f_s\frac{\langle u'v'\rangle}{k}\frac{1+f_d}{1+\frac{3}{2}\frac{\langle v'^2\rangle}{k}f_d}.$$

Equations for the Reynolds normal stresses:

$$u\frac{\partial\langle u'^2\rangle}{\partial x}+v\frac{\partial\langle u'^2\rangle}{\partial y}=\frac{\partial}{\partial y}\left[\left(\nu+C_s\frac{k}{\epsilon}\langle v'^2\rangle\right)\frac{\partial\langle u'^2\rangle}{\partial y}\right]+P_{11}+\Phi_{11}-\epsilon_{11}, \quad (53)$$

$$u\frac{\partial\langle v'^2\rangle}{\partial x}+v\frac{\partial\langle v'^2\rangle}{\partial y}=\frac{\partial}{\partial y}\left[\left(\nu+C_s\frac{k}{\epsilon}\langle v'^2\rangle\right)\frac{\partial\langle v'^2\rangle}{\partial y}\right]+P_{22}+\Phi_{22}-\epsilon_{22}, \quad (54)$$

$$u\frac{\partial\langle w'^2\rangle}{\partial x}+v\frac{\partial\langle w'^2\rangle}{\partial y}=\frac{\partial}{\partial y}\left[\left(\nu+C_s\frac{k}{\epsilon}\langle v'^2\rangle\right)\frac{\partial\langle w'^2\rangle}{\partial y}\right]+P_{33}+\Phi_{33}-\epsilon_{33}, \quad (55)$$

with

$$P_{11}=2P_k, \quad P_{22}=0, \quad P_{33}=0, \quad P_k=-\langle u'v'\rangle\frac{\partial u}{\partial y},$$

$$\Phi_{11}=-C_1\epsilon\left(\frac{\langle u'^2\rangle}{k}-\frac{2}{3}\right)+C_1^w f_w\frac{\epsilon}{k}\langle v'^2\rangle-\frac{2}{3}C_2P_k(2-C_2^w f_w),$$

$$\Phi_{22}=-C_1\epsilon\left(\frac{\langle v'^2\rangle}{k}-\frac{2}{3}\right)-2C_1^w f_w\frac{\epsilon}{k}\langle v'^2\rangle+\frac{2}{3}C_2P_k(1-2C_2^w f_w),$$

$$\Phi_{33}=-C_1\epsilon\left(\frac{\langle w'^2\rangle}{k}-\frac{2}{3}\right)+C_1^w f_w\frac{\epsilon}{k}\langle v'^2\rangle+\frac{2}{3}C_2P_k(1+C_2^w f_w),$$

$$\epsilon_{11}=\epsilon\left[\frac{2}{3}(1-f_s)+f_s\frac{\langle u'^2\rangle}{k}\frac{1}{1+\frac{3}{2}\frac{\langle v'^2\rangle}{k}f_d}\right],$$

$$\epsilon_{22} = \epsilon \left[\frac{2}{3}(1-f_s) + f_s \frac{\langle v'^2 \rangle}{k} \frac{1+3f_d}{1+\frac{3}{2}\frac{\langle v'^2 \rangle}{k} f_d} \right],$$

$$\epsilon_{33} = \epsilon \left[\frac{2}{3}(1-f_s) + f_s \frac{\langle w'^2 \rangle}{k} \frac{1}{1+\frac{3}{2}\frac{\langle v'^2 \rangle}{k} f_d} \right].$$

Equation for the turbulent kinetic energy:

$$u\frac{\partial k}{\partial x} + v\frac{\partial k}{\partial y} = \frac{\partial}{\partial y}\left[\left(\nu + C_s \frac{k}{\epsilon}\langle v'^2 \rangle \right) \frac{\partial k}{\partial y} \right] + P_k - \epsilon. \tag{56}$$

Equation for the dissipation rate of turbulent energy:

$$u\frac{\partial \epsilon}{\partial x} + v\frac{\partial \epsilon}{\partial y} = \frac{\partial}{\partial y}\left[\left(\nu + C_\epsilon \frac{k}{\epsilon}\langle v'^2 \rangle \right) \frac{\partial \epsilon}{\partial y} \right] + C_{\epsilon 1} f_{\epsilon 1} \frac{\epsilon}{k} P_k - C_{\epsilon 2} f_{\epsilon 2} \frac{\epsilon \tilde{\epsilon}}{k} +$$
$$+ C_{\epsilon 3} f_\mu \langle v'^2 \rangle \left(\frac{\partial^2 u}{\partial y^2} \right)^2 + S_{\epsilon 4} + S_l, \tag{57}$$

with

$$\tilde{\epsilon} = \epsilon - 2\nu \left(\frac{\partial \sqrt{k}}{\partial y} \right)^2,$$

$$S_l = \max\left\{ \left[\left(\frac{1}{C_l}\frac{\partial l}{\partial y} \right)^2 - 1 \right] \left(\frac{1}{C_l}\frac{\partial l}{\partial y} \right)^2 ; 0 \right\} \frac{\epsilon \tilde{\epsilon}}{k} A,$$

$$l = \frac{k^{3/2}}{\epsilon},$$

$$S_{\epsilon 4} = C_{\epsilon 4} \frac{\epsilon}{k} \left(\langle v'^2 \rangle - \langle u'^2 \rangle \right) \frac{\partial u}{\partial x}.$$

C_1, C_2, C_1^w, C_2^w are functions which depend on the local turbulence-based Reynolds number, $Re_t = k^2/(\nu\epsilon)$, the invariant parameter of the stress anisotropy tensor, A, and the invariant parameter of the dissipation anisotropy tensor, E.

A is defined as

$$A = 1 - \frac{9}{8}(A_2 - A_3),$$

with $A_2 = a_{ij}a_{ji}, A_3 = a_{ij}a_{jk}a_{ki}$ and $a_{ij} = \langle u_i' u_j' \rangle / k - (2/3)\delta_{ij}$.

E is defined as

$$E = 1 - \frac{9}{8}(E_2 - E_3),$$

with $E_2 = e_{ij}e_{ji}, E_3 = e_{ij}e_{jk}e_{ki}$ and $e_{ij} = \epsilon_{ij}/\epsilon - (2/3)\delta_{ij}$.

The functions in the pressure-strain correlation in the equations for the turbulent stresses are taken as

$$C_1 = C + \sqrt{A}E^2, \qquad C_2 = 0.8\sqrt{A},$$

$$C_1^w = \max\{1 - 0.7C; 0.3\}, \qquad C_2^w = \min\{A; 0.3\},$$

with

$$C = 2.5AF^{1/4}f, \qquad F = \min\{0.6; A_2\}, \qquad f = \min\left\{\left(\frac{Re_t}{150}\right)^{3/2}; 1\right\}.$$

The functions and constants in the equation for the dissipation rate are taken as

$$f_s = 1 - \sqrt{A}E^2, \qquad f_d = \frac{1}{1 + 0.1Re_t},$$
$$C_\epsilon = 0.18, \qquad C_{\epsilon 1} = 1.44, \qquad C_{\epsilon 2} = 1.92, \qquad C_{\epsilon 3} = 0.25, \qquad C_{\epsilon 4} = 2.6,$$
$$f_\mu = 1, \qquad f_{\epsilon 1} = 1, \qquad f_{\epsilon 2} = 1 - \frac{C_{\epsilon 2} - 1.4}{C_{\epsilon 2}} exp\left[-\left(\frac{Re_t}{6}\right)^2\right].$$

Finally, $C_s = 0.22$, $C_l = 2.5$ and

$$f_w = \min\left\{\frac{k^{3/2}}{C_w \epsilon y}; 1.4\right\}$$

with $C_w = 2.5$.

For further details about the various terms included in the equations above, see references Henkes (1997) and Hanjalić *et al.* (1995).

References

Bradshaw, P. 1967 The turbulent structure of equilibrium boundary layers. *J. Fluid Mech.* **29**, 625–645.

Clauser, F. H. 1954 Turbulent boundary layers in adverse pressure gradients. *J. Aero. Sci.* **21**, 91–108.

Coleman, G. N. & Spalart, P. R. 1993 Direct numerical simulation of a small separation bubble. In *Near-Wall Turbulent Flows* (eds. R. So, C. Speziale & B. Launder), pp. 227–286. Elsevier.

Durbin, P. A. & Belcher, S. E. 1992 Scaling of adverse-pressure-gradient turbulent boundary layers. *J. Fluid Mech.* **238**, 699–722.

Fernholz, H. H. & Finley, P. J. 1996 The incompressible zero-pressure-gradient turbulent boundary layer: An assessment of the data. *Prog. Aerospace Sci.* **32**, 245–311.

George, W. K. & Castillo, L. 1993 Boundary layers with pressure gradient: another look at the equilibrium boundary layer. In *Near-Wall Turbulent Flows* (eds. R. M. C. So, C. G. Speziale & B. E. Launder), pp. 901–910. Elsevier.

Hanjalić, K., Jakirlić, S. & Hadžić, I. 1995 Computation of oscillating turbulent flows at transitional *Re*-numbers. In *Turbulent Shear Flows 9* (eds. F. Durst, N. Kasagi & B. E. Launder), pp. 323–342. Springer-Verlag.

Hanjalić, K. & Launder, B. E. 1980 Sensitizing the dissipation equation to irrotational strains. *J. Fluids Eng.* **102**, 34–40.

Head, M. R. 1976 Equilibrium and near-equilibrium turbulent boundary layers. *J. Fluid Mech.* **73**, 1–8.

Henkes, R. A. W. M. 1997 Comparison of turbulence models for attached boundary layers relevant to aeronautics. *Appl. Sci. Res.* **57**, 43–65.

Henkes, R. A. W. M. 1998 Scaling of equilibrium boundary layers under adverse pressure gradient using turbulence models. *AIAA J.* **36**, 320–326.

Henkes, R. A. W. M., Skote, M. & Henningson, D. S. 1997 Application of turbulence models to equilibrium boundary layers under adverse pressure gradient. Eleventh Symposium on Turbulent Shear Flows, Grenoble, France.

Henningson, D. S. & Lundbladh, A. 1995 Evaluation of turbulence models from direct numerical simulations of turbulent boundary layers. FFA-TN 1995-09, Aeronautical Research Institute of Sweden, Bromma.

Lundbladh, A., Henningson, D. S. & Johansson, A. V. 1992 An efficient spectral integration method for the solution of the Navier-Stokes equations. FFA-TN 1992-28, Aeronautical Research Institute of Sweden, Bromma.

Lundbladh, A., Schmid, P. J., Berlin, S. & Henningson, D. S. 1994 Simulation of bypass transition in spatially evolving flows. Proceedings of the AGARD Symposium on Application of Direct and Large Eddy Simulation to Transition and Turbulence, AGARD-CP-551.

Mellor, G. L. & Gibson, D. M. 1966 Equilibrium turbulent boundary layers. *J. Fluid Mech.* **24**, 225–253.

Na, Y. & Moin, P. 1996 Direct numerical simulation of studies of turbulent boundary layers with adverse pressure gradient and separation. *Tech. Rep.* TF-68. Thermosciences Division, Department of Mechanical Engineering, Stanford University.

Nagano, Y., Tagawa, M. & Tsuji, T. 1992 Effects of adverse pressure gradients on mean flows and turbulence statistics in a boundary layer. In *Turbulent Shear Flows 8* (eds. F. Durst, R. Friedrich, B. E. Launder, F. W. Schmitd, U. Schumann & J. H. Whitelaw), pp. 7–21. Springer-Verlag.

Nordström, J., Nordin, N. & Henningson, D. S. 1999 The fringe region technique and the fourier method used in the direct numerical simulation of spatially evolving viscous flows. *SIAM J. Sci. Comp.* **20** (4), 1365–1393.

Rotta, J. C. 1962 Turbulent boundary layers in incompressible flow. *Prog. Aerospace Sci.* **2**, 3–219.

Samuel, A. E. & Joubert, P. N. 1974 A boundary layer developing in an increasingly adverse pressure gradient. *J. Fluid Mech.* **66**, 481–505.

Schofield, W. H. 1981 Equilibrium boundary layers in moderate to strong adverse pressure gradients. *J. Fluid Mech.* **113**, 91–122.

Skåre, P. E. & Krogstad, P.-Å. 1994 A turbulent equilibrium boundary layer near separation. *J. Fluid Mech.* **272**, 319–348.

Spalart, P. R. 1988 Direct simulation of a turbulent boundary layer up to $Re_\theta = 1410$. *J. Fluid Mech.* **187**, 61–98.

Spalart, P. R. & Coleman, G. N. 1997 Numerical study of a separation bubble with heat transfer. *European J. Mechanics B/Fluids* **16**, 169.

Spalart, P. R. & Leonard, A. 1987 Direct numerical simulation of equilibrium turbulent boundary layers. In *Turbulent Shear Flows 5* (eds. F. Durst, B. E. Launder, J. L. Lumley, F. W. Schmitd & J. H. Whitelaw), pp. 234–252. Springer-Verlag.

Spalart, P. R. & Watmuff, J. H. 1993 Experimental and numerical study of a turbulent boundary layer with pressure gradients. *J. Fluid Mech.* **249**, 337–371.

Stratford, B. S. 1959*a* An experimental flow with zero skin friction throughout its region of pressure rise. *J. Fluid Mech.* **5**, 17–35.

Stratford, B. S. 1959*b* The prediction of separation of the turbulent boundary layer. *J. Fluid Mech.* **5**, 1–16.

Tennekes, H. & Lumley, J. L. 1972 *A First Course in Turbulence*. The MIT Press.

Townsend, A. A. 1960 The development of turbulent boundary layers with negligible wall stress. *J. Fluid Mech.* **8**, 143–155.

Townsend, A. A. 1976 *The Structure of Turbulent Shear Flow*. Cambridge University Press.